PHYSICAL SCIENCE

Low-energy structural dynamics of ferroelectric domain walls in hexagonal rare-earth manganites

Xiaoyu Wu,[1] Urko Petralanda,[2] Lu Zheng,[1] Yuan Ren,[1] Rongwei Hu,[3] Sang-Wook Cheong,[3]* Sergey Artyukhin,[2]* Keji Lai[1]*

Domain walls (DWs) in ferroic materials, across which the order parameter abruptly changes its orientation, can host emergent properties that are absent in the bulk domains. Using a broadband (10^6 to 10^{10} Hz) scanning impedance microscope, we show that the electrical response of the interlocked antiphase boundaries and ferroelectric DWs in hexagonal rare-earth manganites (h-RMnO$_3$) is dominated by the bound-charge oscillation rather than free-carrier conduction at the DWs. As a measure of the rate of energy dissipation, the effective conductivity of DWs on the (001) surfaces of h-RMnO$_3$ at gigahertz frequencies is drastically higher than that at dc, whereas the effect is absent on surfaces with in-plane polarized domains. First-principles and model calculations indicate that the frequency range and selection rules are consistent with the periodic sliding of the DW around its equilibrium position. This acoustic wave–like mode, which is associated with the synchronized oscillation of local polarization and apical oxygen atoms, is localized perpendicular to the DW but free to propagate along the DW plane. Our results break the ground to understand structural DW dynamics and exploit new interfacial phenomena for novel devices.

INTRODUCTION

Domain walls (DWs) in ferroic materials are the natural interfaces separating domains with different order parameters. Their dynamic responses to external stimuli, which have received tremendous research interest in recent years, play an essential role in determining the material properties. In ferromagnets, for example, the supersonic motion of DWs driven by a spin-polarized current leads to the exciting development of magnetic racetrack memories (*1*, *2*). The periodic motion of magnetic DWs around the equilibrium position can be induced by a radio-frequency current, which has been studied to extract the effective DW mass and to enable low-current device operations (*3*). For the electric counterpart, the propagation of ferroelectric DWs under a dc bias has been extensively investigated to understand the switching mechanism (*4*–*6*). On the other hand, the dynamics of ferroelectric DWs under ac electric fields have not been thoroughly analyzed. Although signatures of ferroelectric DW oscillation [for example, the dielectric dispersion at the microwave regime (*7*–*12*)] have long been noticed by the scientific community, little is known on the nanoscale dynamics down to the single DW level, because conventional bulk measurements inevitably sum up the responses from domains with different polarizations and walls with different orientations (*13*, *14*). Spatially resolved studies that address the nanoscale ac response are therefore crucial to explore the underlying physics of these low-energy excitations localized at the DWs, which may be useful for nanoelectronic applications (*15*).

The electrical probing of ferroelectric DW response at the megahertz to gigahertz frequency (f) regime may be complicated by the presence of mobile carriers. To maintain a spontaneous polarization, the bulk ferroelectric domains are usually highly resistive. However, ferroelectric DWs can host anomalous electrical conduction because of the redistribution of carriers, which has been observed by conductive atomic force microscopy (C-AFM) studies (*16*–*22*). The difference of dc conductivity between DWs and domains is usually large for charged walls, where free carriers are accumulated or depleted because of the polarization discontinuity (*23*, *24*), and small for nominally uncharged walls, where secondary effects, such as the flexoelectric coupling (*25*) or the reduction of bandgap (*16*), may take place. In addition, defects, such as excess oxygen or oxygen vacancies, can also affect the conductivity of DWs and domains through the change of carrier density (*26*–*29*). Because the contribution from mobile carriers and bound charges at the DWs to the energy loss cannot be separated in a single-f measurement, a broadband study is of vital importance to understand the dynamic response of ferroelectric DWs.

Here, we report the multi-f impedance microscopy experiments and theoretical analysis on the DWs of single-crystalline hexagonal rare-earth manganites (h-RMnO$_3$; R = Sc, Y, Dy–Lu). The h-RMnO$_3$ family of materials are geometric improper ferroelectrics in that the spontaneous polarization P along the hexagonal c axis is a by-product of the trimerization of the MnO$_5$ polyhedra setting in at the structural phase transition around 1000 K (*30*). The primary order parameter, a two-dimensional (2D) vector with length Q and azimuthal angle ϕ, describes the shift of apical oxygen atoms when the MnO$_5$ polyhedra tilt. The coupling between the polarization and trimerization leads to a firm clamping of ferroelectric DWs and structural antiphase boundaries (*31*, *32*). We show that the effective conductivity of DWs on the (001) surface at gigahertz frequencies is drastically higher than that at dc, whereas the effect is absent on surfaces with in-plane polarized domains. Theoretical calculations indicate that the observed behavior is consistent with the dielectric loss due to periodic sliding of the DW around its equilibrium position, that is, the synchronized oscillation of local polarization and apical oxygen atoms. Our results represent a major milestone in understanding the structural DW dynamics in complex systems.

[1]Department of Physics, University of Texas at Austin, Austin, TX 78712, USA. [2]Quantum Materials Theory, Istituto Italiano di Tecnologia, Genova, Italy. [3]Rutgers Center for Emergent Materials and Department of Physics and Astronomy, Rutgers University, Piscataway, NJ 08854, USA.
*Corresponding author. Email: sangc@physics.rutgers.edu (S.-W.C.); sergey.artyukhin@iit.it (S.A.); kejilai@physics.utexas.edu (K.L.)

RESULTS

Multimode microscopy on (001) YMnO$_3$

Our multimode imaging setup on a commercial AFM platform is schematically illustrated in Fig. 1A. We first discuss the results on the (001) surface of as-grown YMnO$_3$ samples. With no corresponding topographic

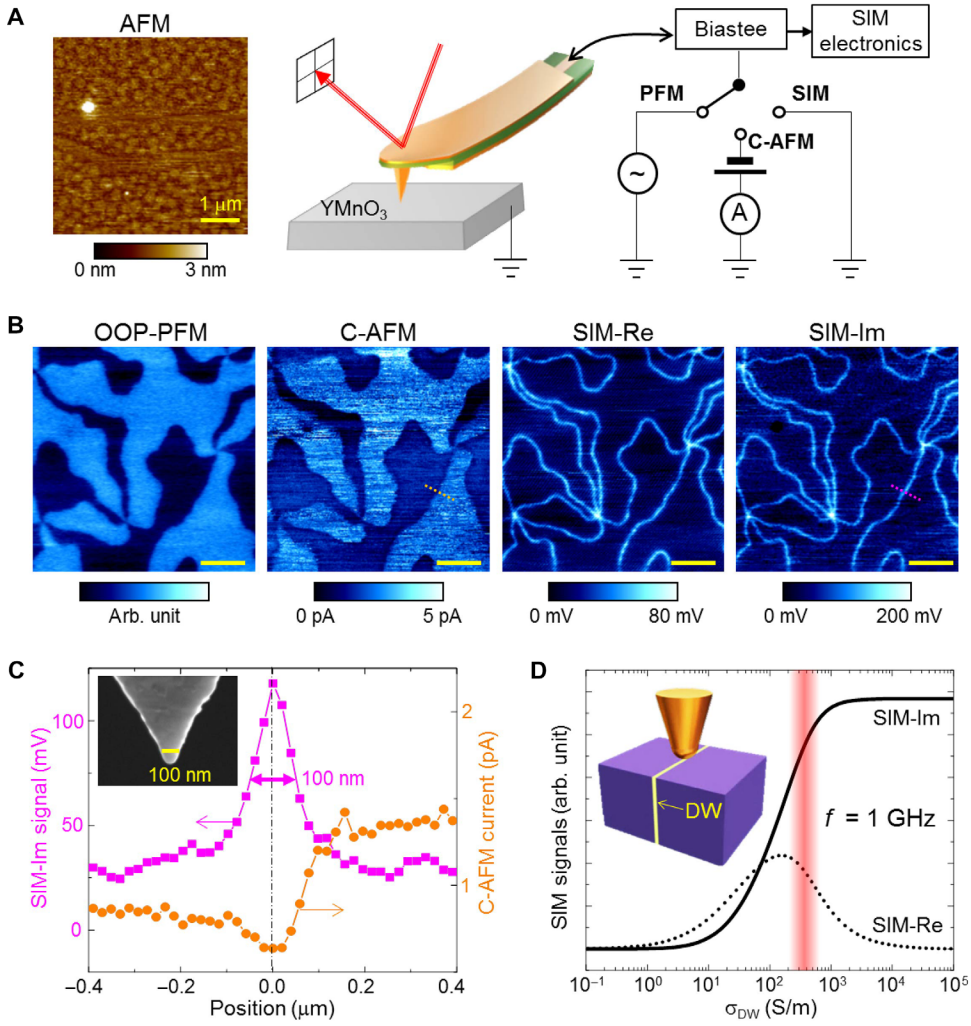

Fig. 1. Multimode microscopy on (001) $YMnO_3$. (**A**) Schematic of the experimental setup. The shielded cantilever probe is connected to the SIM electronics via a bias tee, through which a low-frequency ac voltage (95 kHz, 5 V) for PFM or a dc bias (−5 V) for C-AFM can be applied to the tip. The AFM image on the left shows the surface topography of (001) $YMnO_3$. (**B**) OOP-PFM, C-AFM, SIM-Re, and SIM-Im (f = 1 GHz) images acquired on the same area. Arb. unit, arbitrary unit. Scale bars, 1 μm. (**C**) SIM-Im (pink) and C-AFM (orange) line profiles across a single DW centered at position 0.0 μm and labeled as dashed lines in (B). The full width at half maximum of 100 nm is comparable to the tip diameter, as shown in the scanning electron microscopy image in the inset. (**D**) Simulated SIM signals as a function of the effective DW conductivity. The measured DW signals with a ratio of SIM-Re/Im ~0.4 (shaded in red) are consistent with σ_{DW} ~400 S/m. The inset shows the tip-sample geometry for the FEA.

features, the cloverleaf-like domain patterns are vividly seen in the out-of-plane (OOP) piezoresponse force microscopy (PFM) data in Fig. 1B. Because of its semiconducting bandgap of ~1.5 eV and slight p-doping from interstitial oxygen (*28*) during the growth, the as-grown $YMnO_3$ in our experiment shows a room temperature conductivity σ_{bulk} of ~0.3×10^{-3} S/m (fig. S1) (*31*, *33*, *34*). This bulk conduction is further modulated by the different surface band bending between up- and down-polarized domains, giving rise to the domain contrast in the C-AFM image under a tip bias of −5 V (*31*, *34*). In contrast to the uncharged walls in other ferroelectrics (*16*–*18*), it was found that the charge-neutral DWs on the (001) $YMnO_3$ surface are more resistive than the adjacent domains (*31*). Because the paraelectric phase of $YMnO_3$ is more insulating than its ferroelectric phase, it was suggested that the dc behavior of the DWs closely resembles the corresponding high-temperature, high-symmetry states (*31*).

Different from the dc C-AFM, the scanning impedance microscope (SIM) (*35*, *36*) working at f = 1 GHz measures the local complex permittivity of the material with a spatial resolution of ~100 nm, which is determined by the tip diameter d (fig. S2). The input excitation power is on the order of 10 μW (*35*), corresponding to a low-gigahertz tip voltage of ~0.1 V. The electric field ~10 kV/cm at the tip apex is too small to cause ferroelectric switching of the $YMnO_3$ domains (*26*, *27*, *31*). The output SIM-Re and SIM-Im signals are proportional to the real and imaginary parts of the tip-sample admittance, respectively. The SIM images acquired on the same area as above are also displayed in Fig. 1B. Strikingly, although the DWs are the least-conductive objects on the (001) surface at zero frequency, they exhibit much higher SIM signals than do the bulk domains, as seen from the line profiles in Fig. 1C. Note that because the tip diameter is much larger than the size of the vortex cores (*37*), the high SIM signals at the cores may be a resolution-limited effect due to the summation of adjacent DW signals. Therefore, we will not analyze the SIM data on the vortices.

To interpret the SIM data as physical quantities, we use finite element analysis (FEA) to simulate the DW response at gigahertz frequencies (*36*). Near the surface of plate-like $YMnO_3$ crystals, the DWs tend

to be perpendicular to the surface for a depth (h) of several micrometers (*38*), that is, $h \gg d$. As a result, we can model the DW as a vertical narrow slab sandwiched between adjacent domains. To compare results at different frequencies, we characterize the total dielectric loss at the DWs, including both contributions from mobile carriers and DW dynamics, by the effective DW ac conductivity σ_{DW}^{ac}. Detailed procedures of the FEA modeling are found in fig. S3. The simulated SIM signals as a function of σ_{DW}^{ac} are plotted in Fig. 1D. Compared with the FEA result, the measured DW contrast corresponds to $\sigma_{DW}^{ac} \approx 400$ S/m, which is five to six orders of magnitude higher than σ_{DW}^{dc}. The electrical response of $YMnO_3$ DWs is therefore qualitatively different from that of the ferroelectric lead zirconate (PZT) (*39*) and the magnetic insulator $Nd_2Ir_2O_7$ (*40*), where the DWs are more conductive than domains at both dc and gigahertz frequencies.

Control experiments on other h-*R*MnO_3 samples

To investigate the generality of the observed behavior, we have also performed control experiments on other h-*R*MnO_3 samples. As shown in Fig. 2A, the same DW contrast in SIM data is seen on the (001) surface of $ErMnO_3$, suggesting that the effect is insensitive to the variation of rare-earth elements. However, the situation is rather different on the h-*R*MnO_3 surfaces with in-plane polarized domains. In Fig. 2B, no DW contrast in the SIM images is observed on the cleaved (110) $HoMnO_3$ crystal. In addition, we cut two pieces from the same $HoMnO_3$ crystal and polished the (001) surface for one sample and the (100) surface for the other. As displayed in fig. S4, the appearance and absence of SIM contrast of DWs are again observed on the (001) and (100) surfaces, respectively.

DWs inside h-*R*MnO_3 form a complex network that permeates the bulk of the material (*41*). On the (110) and (100) surfaces with in-plane polarization, charged DWs are stabilized by the interlocking of the ferroelectric and antiferrodistortive orders. Previous C-AFM work on these surfaces showed that σ_{DW}^{dc} varies continuously as the neighboring domains change from "tail-to-tail" to "head-to-head" configurations, presumably because of the accumulation or depletion of p-type carriers (*42*, *43*). On the other hand, only moderate conductance difference between domains and DWs (within an order of magnitude) is measured on these surfaces (*42*). Compared with the FEA results in Fig. 1D, the contribution due to mobile carriers on the charged walls ($\sigma_{DW}^{dc} \ll 1$ S/m) is still too small to be detected by the SIM. As a result, the missing DW contrast on the (110) and (100) surfaces at $f = 1$ GHz indicates that the contribution from dipolar loss to the local energy dissipation is also negligible in crystal planes parallel to the polarization axis.

Frequency-dependent DW response

To further explore the unusual ac response of DWs on (001) $YMnO_3$, we construct multiple SIM electronics to cover a broad spectrum ranging from 10^6 to 10^{10} Hz (fig. S5). Selected SIM images with clear DW contrast are shown in Fig. 3 (A to D) (more in fig. S6). Because of different settings, such as input power, amplifier gains, and impedance-match sections of the electronics, the absolute SIM signals cannot be directly compared between different frequencies. Moreover, the SIM output is strongly dependent on the condition of the tip apex, as evident from the simulation results in Fig. 3E. We have therefore taken the ratios between SIM-Re and SIM-Im signals, which not only cancel out the circuit-dependent factors but also show much weaker dependence on the tip diameter (Fig. 3F), for quantitative analysis. As shown in fig. S7, repeated line scans were also taken across several DWs to improve the signal-to-noise ratio at each f. In Fig. 3G, the SIM-Re/Im data are plotted together with the constant σ_{DW}^{ac} contours from the FEA simulation. Within the experimental errors in Fig. 3H, the effective DW conductivity rises rapidly from nearly zero at dc to ~500 S/m above 1 GHz and develops a feature not inconsistent with a broad peak around 3 to 5 GHz, although the cutoff frequency at 10 GHz prevents us from resolving the full resonance–like peak. Given the very small contribution from the Drude conduction of mobile carriers, it is obvious that the bound-charge motion at the DWs, which is microscopically equivalent to the vibration of DW position, on the (001) surface of h-*R*MnO_3 is responsible for the pronounced ac loss observed in our experiment.

Theoretical analysis of DW dynamics in h-*R*MnO_3

The starting point to analyze the lattice dynamics in h-*R*MnO_3 is to understand its nonuniform trimerization textures, which were first explained within the long-wavelength Landau theory, using parameters extracted from ab initio calculations (*44*). Density functional theory (DFT) calculations predict the lowest optical phonon at ~2 THz (*44*, *45*), well above the characteristic frequency in our experiment. On the other hand, the presence of DWs breaks the continuous translational symmetry

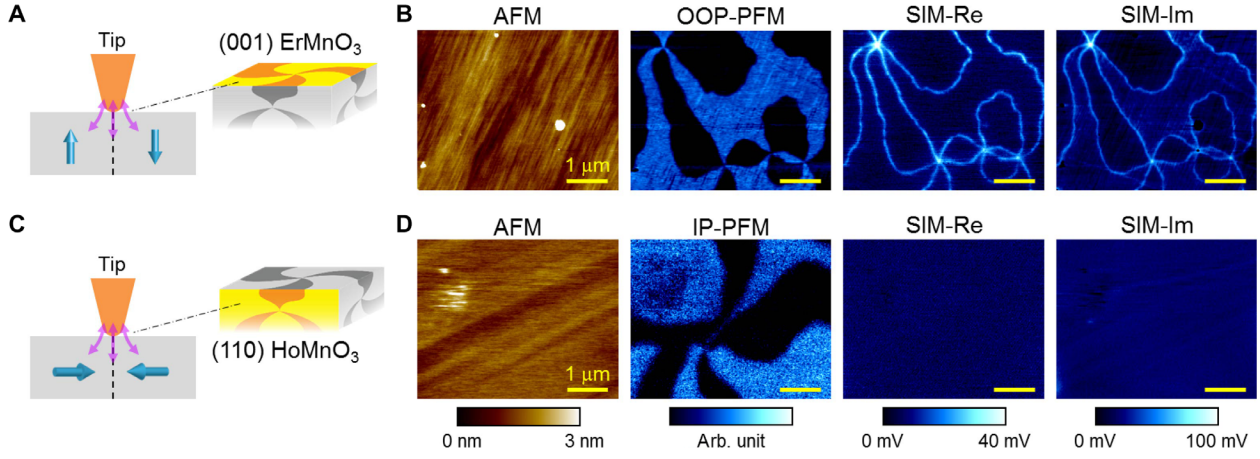

Fig. 2. SIM experiments on other h-*R*MnO_3. (**A**) Schematic representation of the tip electric fields (pink) and the OOP polarization (blue) on the highlighted (001) $ErMnO_3$ surface. (**B**) AFM, OOP-PFM, SIM-Re, and SIM-Im ($f = 1$ GHz) images acquired on (001) $ErMnO_3$. Clear DW contrast can be seen in the SIM data. (**C**) and (**D**) are the same as (A) and (B), except that the schematic and the data are for (110) $HoMnO_3$, showing clear domain contrast in the in-plane (IP) PFM but no DW contrast in the SIM images. Scale bars, 1 μm.

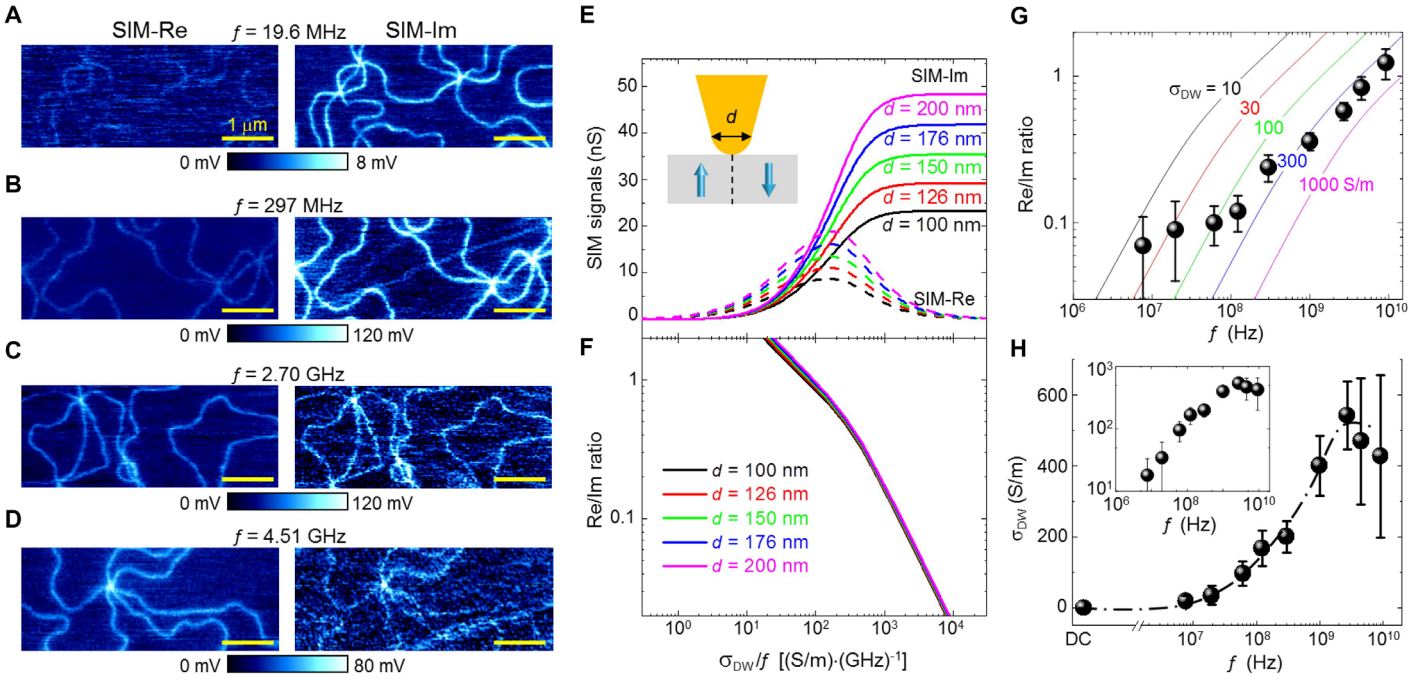

Fig. 3. Frequency-dependent DW response. (**A** to **D**) SIM images on (001) $YMnO_3$ at selected frequencies. Scale bars, 1 μm. Simulated SIM signals (**E**) and SIM-Re/Im ratios for different tip diameters (**F**), showing weak dependence on the exact tip condition when the Re/Im ratio is calculated. Note that the *x* axis is σ_{DW}/f, that is, the simulation is invariant when σ_{DW} is scaled by the frequency. (**G**) SIM-Re/Im ratio of the DW signals as a function of *f* in a log-log plot. The constant σ_{DW} contours at 10, 30, 100, 300, and 1000 S/m are also plotted in the graph. (**H**) *f*-dependent σ_{DW} of the (001) $YMnO_3$ DWs. The dash-dot line is a guide to the eyes. The inset shows the same data in the log-log scale.

and introduces a mode associated with the periodic DW sliding around its equilibrium position, whose energy approaches zero in the continuum model. When the DW width λ is comparable to the lattice constant *a*, the sliding mode acquires a gap due to the discrete translational symmetry of the lattice. The essential physics of DW dynamics can be captured by a simplified 1D model Hamiltonian

$$H = \sum_r \frac{(\dot{A}_r)^2}{2m} + b(A_r^2 - 1)^2 + \frac{c}{2}(A_r - A_{r+\delta})^2 - EA \qquad (1)$$

where the four terms represent the kinetic energy of the local mode A_r at site *r* with mass *m*, the local double-well potential, the nearest-neighbor interaction, and the interaction between the local mode and oscillating external field *E*, respectively. In the equilibrium, the center of the DW locates between two adjacent sites, as shown in Fig. 4A, so that the mode amplitude at every site is close to the minimum of the ferroelectric double-well potential. When moving to a neighboring unit cell, the DW passes through an intermediate configuration in Fig. 4B, where it is centered at the site. The mode amplitude of this configuration corresponds to a maximum of the potential and a high total energy. The energy difference between these two configurations gives rise to the Peierls-Nabarro barrier (*46*, *47*) in Fig. 4C that needs to be overcome to flip the polarization of a unit cell and move the DW to the adjacent cell. In our SIM experiment, the excitation tip voltage, thus the external field *E*, is too low to cause any ferroelectric switching. As a result, we only need to consider the linear response of this model Hamiltonian.

The solution of Eq. 1 reveals two nondispersive modes localized perpendicular to the DW plane, along with the continuous spectrum of bulk phonons, as shown in Fig. 4D. The lowest-energy mode (Fig. 4E) corresponds to oscillations of the DW position, whereas the higher-energy breathing mode (Fig. 4F) corresponds to oscillations of the DW width. As seen in Fig. 4G, the frequency of the DW sliding mode rapidly decreases with increasing λ and approaches zero for $\lambda \gg a$, consistent with the free DW sliding in the continuum theory. The nearly exponential dependence of the resonance frequency on λ makes it difficult to precisely calculate the frequency from an approximate model, but it is still possible to estimate it by the order of magnitude. This simple model thus illustrates how the low-energy gigahertz-scale mode emerges from the terahertz phonon spectrum.

Now, we extend the abovementioned model to incorporate the principal trimerization amplitude (*Q*), angle (ϕ), and polarization (*P*) modes in $YMnO_3$. Because the DW vibration occurs at a frequency much lower than the optical phonons, it is within the error bars of the conventional frozen phonon calculations (*48*). To provide a quantitative estimate, we use the discretized version of the model used by Artyukhin *et al.* (*44*), where the effective masses and intersite couplings are extracted from the phonon dispersion calculated within DFT. Detailed calculations on the full model Hamiltonian of a 120-site supercell with a DW centered in the middle are included in fig. S8. The DW energy centered at the Mn sites is lower than that in between the sites, again giving rise to the washboard-like Peierls-Nabarro barrier. The atomistic view of $YMnO_3$ in Fig. 5A shows the synchronized oscillation of apical oxygen atoms and the local polarization during the periodic DW sliding. In Fig. 5B, the ground-state configuration by minimizing the model Hamiltonian is plotted for *Q*, ϕ, and *P*. The calculated phonon dispersion can be visualized by the phonon spectral function in Fig. 5C, where the damping is estimated from optical experiments (*49*). Similar to the simplified model, the spectrum contains the usual dispersive phonons originated

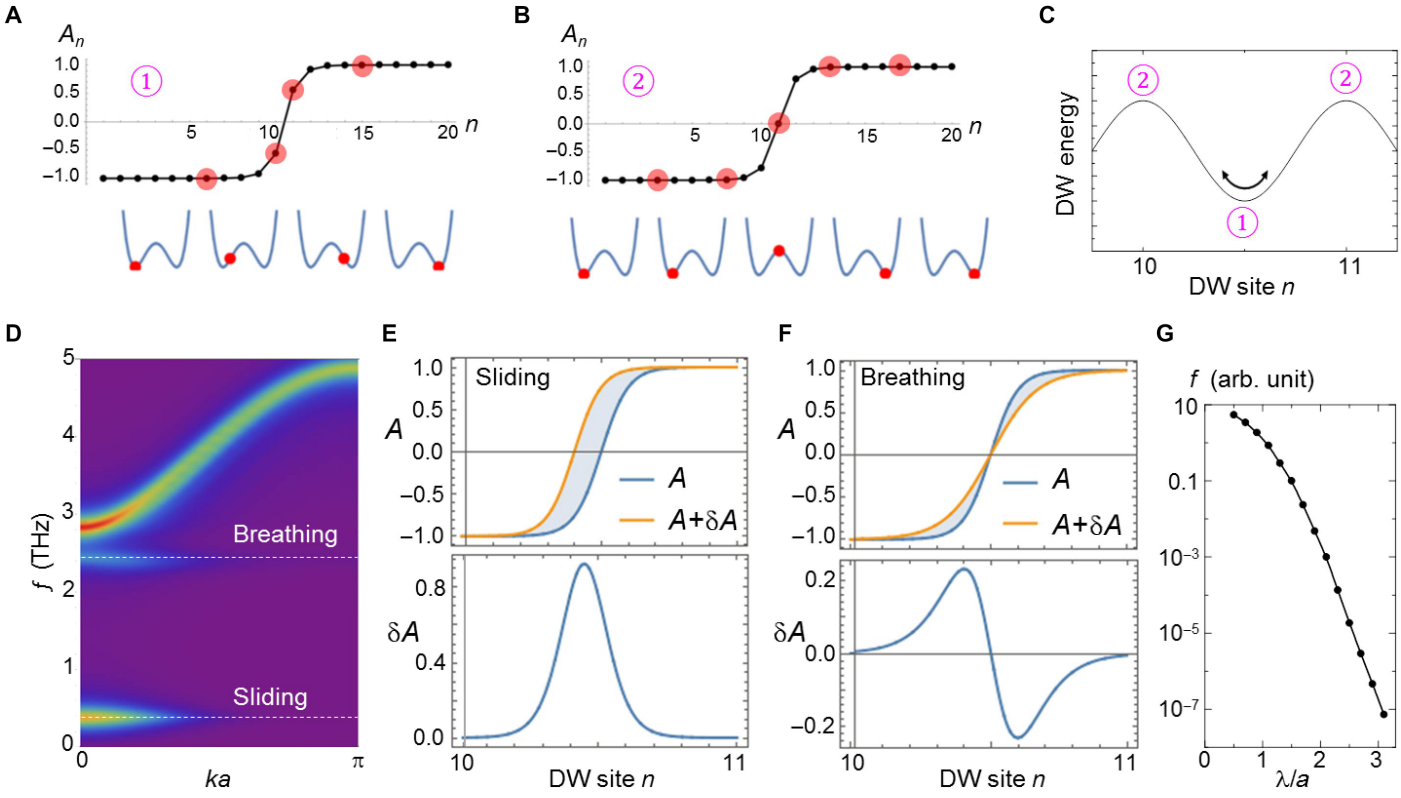

Fig. 4. Periodic DW sliding in the simplified model. (**A**) Ground-state configuration of the simplified Hamiltonian (1), with the DW centered between two Mn sites. (**B**) High-energy configuration when the DW is centered at a Mn site. The schematics in (A) and (B) show the corresponding on-site energies in the double-well potential. (**C**) Washboard-like potential when the center of the DW slides across different sites. (**D**) Phonon spectral function in this simple model, showing the nondispersive sliding mode at the lowest energy, the breathing mode at a higher energy, and the dispersive bulk phonon branch. (**E**) Mode texture for a lateral shift of the DW position (top) and the corresponding DW sliding mode (bottom). (**F**) Mode texture for an increase of the DW width (top) and the corresponding DW breathing mode (bottom). (**G**) Dependence of the DW oscillation frequency on its width.

from the Γ_2^- and K_3 modes in the $P6_3/mmc$ space group (*45*) and nondispersive branches, the lowest of which corresponds to the localized DW oscillating mode. In Fig. 5D, the order parameter oscillation amplitudes at the lattice sites are plotted for both a regular phonon and the localized mode. Note that our 1D model calculations only capture the bottom of the phonon bands, that is, phonons with zero wave vector in the DW plane. In real 3D crystals, the vibration of local polarization and oxygen atoms can still propagate with nonzero wave vectors within the DW plane, resembling the acoustic waves in elastic media. The bandwidth of such a DW–acoustic wave mode is determined by the intersite coupling strength and is therefore of the same order as the bandwidth of the Γ_2^- and K_3 modes in the bulk.

DISCUSSION

Comparisons between our experimental and theoretical results strongly suggest that the ac response of the h-RMnO$_3$ DWs is associated with the DW oscillation mode. First, for DWs on the (001) surface, the vertical component of the oscillating E field from the SIM tip is aligned with either up- or down-polarized domains in each half-cycle, leading to the periodic motion of the apical oxygen atoms coupled with local polarization and, thus, the ac dielectric loss. In contrast, the coupling between the tip E fields and the DW motion on the (110) and (100) surfaces is negligible because of E being mostly orthogonal to P. Such a "selection rule" is seen in Fig. 2 and fig. S4. Second, although the error bars of a full ab initio calculation for all 3 × 30 h-RMnO$_3$ phonons can mask the low-energy mode, our model Hamiltonian, taking the essential Q, ϕ, and P modes into account, provides an estimate of its frequency that falls into the gigahertz regime. Further development of the model, such as the inclusion of the next nearest-neighbour interaction and more phonon modes, may allow a more quantitative comparison with the experiment. Third, our generic analysis of the low-energy DW vibration may explain the dielectric dispersion observed in many ferroelectrics (*7*–*12*). Future experiments on materials with a characteristic frequency well within the range of our SIM, for example, 0.1 to 1 GHz, will allow us to resolve the resonance-like peak (similar to Fig. 3H), which contains important information, such as the DW effective mass. Last, our model calculations suggest the possible presence of an acoustic mode localized perpendicular to the wall but free to propagate within the DW plane. If confirmed by future experiments, this low-energy excitation, in analogy to the magnonic wave traveling along the magnetic DWs (*50*) and to the surface acoustic wave traveling on the surface of piezoelectric materials (*51*), may be exploited for nanoelectronic applications.

To summarize, by using broadband impedance microscopy, we have observed the drastic increase of effective DW conductivity from dc to microwave frequency on the (001) surfaces of hexagonal manganites, although the effect is absent on surfaces with in-plane polarized domains. First-principles and model calculations indicate that the DW oscillation, rather than the presence of free carriers, is responsible for the ac energy loss and selection rules. Thus, ferroelectric DWs, with their

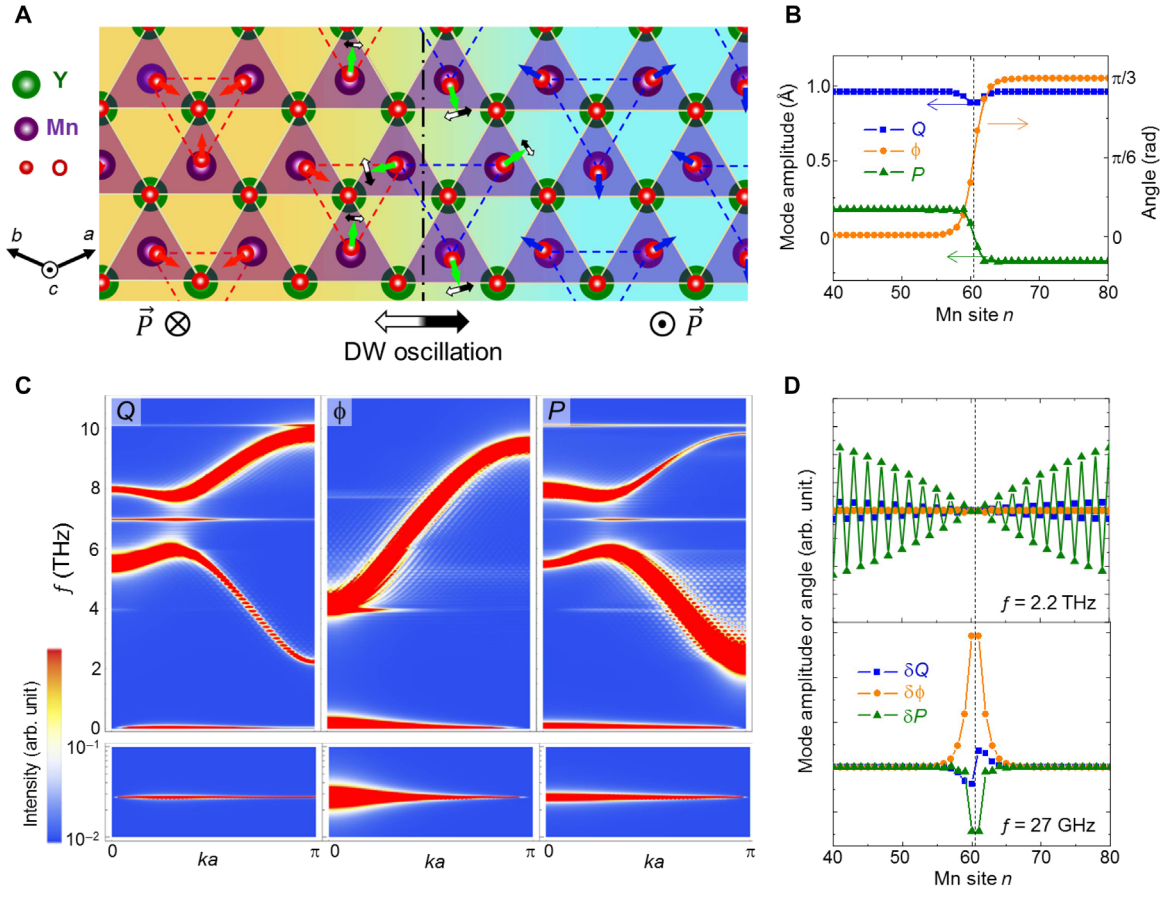

Fig. 5. DW dynamics revealed by first principles–based model calculations. (**A**) Atomistic view of $YMnO_3$ in the (001) plane across the interlocked antiphase boundary and ferroelectric DW. The MnO_5 polyhedra are shaded in purple. The displacements of apical oxygen atoms in the down-domain (left), DW (middle), and up-domain (right) regions are displayed by red, green, and blue arrows, respectively. The trimers are indicated by dashed triangles. The black and white double-headed arrows illustrate the amplitudes and directions of the periodic DW sliding. (**B**) Ground-state configuration of the three order parameters across the DW obtained by minimizing the model Hamiltonian. (**C**) Phonon spectral function projected to the *Q*, ϕ, and *P* modes. The ripples are due to the finite size (120 sites) of the supercell. The lower panels in the log scale show the spectral intensity of the low-energy nondispersive branch. (**D**) Real-space oscillation of δ*Q*, δϕ, and δ*P* for a regular dispersive phonon at the terahertz range (top) and the localized DW sliding mode at the gigahertz range (bottom).

own rich excitations, offer a new playground to explore emergent interfacial phenomena that are not present in bulk domains.

MATERIALS AND METHODS

Material preparation

Plate-like single crystals of h-$RMnO_3$ with an in-plane size of a few millimeters were grown by a flux method with a mixture of h-$RMnO_3$ polycrystalline powder and Bi_2O_3 (molar ratio, 1:6), slowly cooled from 1280° to 970°C at a rate of 2°C/hour. To prepare type-I ferroelectric domains of h-$RMnO_3$, single crystals of h-$RMnO_3$ were annealed at 1180°C, above its T_C, in Ar atmosphere and slowly cooled to 1000°C in 2 hours and then quenched to room temperature to avoid surface oxidation at lower temperatures.

Scanning impedance microscopy

The multimode imaging experiments, including SIM, PFM, and C-AFM, were performed in an AFM platform (XE-70) from Park Systems. Customized electronics were used for impedance imaging at frequencies above 50 MHz. The HF2LI lock-in amplifier from Zurich Instruments was configured to perform SIM at frequencies below 50 MHz. The DLPCA-200 current amplifier from FEMTO Inc. was used for the C-AFM imaging. The microfabricated shielded probes are commercially available from PrimeNano Inc. Finite element modeling was performed by using the commercial software COMSOL 4.4.

SUPPLEMENTARY MATERIALS

Supplementary material for this article is available at http://advances.sciencemag.org/cgi/content/full/3/5/e1602371/DC1

section S1. dc conductivity of h-$RMnO_3$
section S2. SIM electronics and the calibration process
section S3. FEA of the tip-sample interaction
section S4. SIM data on polished $HoMnO_3$ samples
section S5. SIM circuits and impedance match at different frequencies
section S6. More SIM data at various frequencies
section S7. Repeated line scans for improving the signal-to-noise ratio
section S8. Details of the full model calculations
fig. S1. Measurement of the dc resistivity of $YMnO_3$.
fig. S2. SIM electronics and the calibration process.
fig. S3. FEA of the tip-sample interaction.
fig. S4. SIM data on polished $HoMnO_3$ samples.

fig. S5. Impedance-match sections at different frequencies.
fig. S6. SIM images at various frequencies.
fig. S7. SIM experiments with repeated line scans.
fig. S8. First principles–based model calculations.
References (*52*–*57*)

REFERENCES AND NOTES

1. S. S. P. Parkin, M. Hayashi, L. Thomas, Magnetic domain-wall racetrack memory. *Science* **320**, 190–194 (2008).
2. M. Hayashi, L. Thomas, R. Moriya, C. Rettner, S. S. P. Parkin, Current-controlled magnetic domain-wall nanowire shift register. *Science* **320**, 209–211 (2008).
3. E. Saitoh, H. Miyajima, T. Yamaoka, G. Tatara, Current-induced resonance and mass determination of a single magnetic domain wall. *Nature* **432**, 203–206 (2004).
4. Y.-H. Shin, I. Grinberg, I.-W. Chen, A. M. Rappe, Nucleation and growth mechanism of ferroelectric domain-wall motion. *Nature* **449**, 881–884 (2007).
5. S. V. Kalinin, A. N. Morozovska, L.-Q. Chen, B. J. Rodriguez, Local polarization dynamics in ferroelectric materials. *Rep. Prog. Phys.* **73**, 056502 (2010).
6. C. T. Nelson, P. Gao, J. R. Jokisaari, C. Heikes, C. Adamo, A. Melville, S.-H. Baek, C. M. Folkman, B. Winchester, Y. Gu, Y. Liu, K. Zhang, E. Wang, J. Li, L.-Q. Chen, C.-B. Eom, D. G. Schlom, X. Pan, Domain dynamics during ferroelectric switching. *Science* **334**, 968–971 (2011).
7. C. Kittel, Domain boundary motion in ferroelectric crystals and the dielectric constant at high frequency. *Phys. Rev.* **83**, 458 (1951).
8. M. Maglione, R. Böhmer, A. Loidl, U. T. Höchli, Polar relaxation mode in pure and iron-doped barium titanate. *Phys. Rev. B Condens. Matter* **40**, 11441–11444 (1989).
9. G. Arlt, U. Böttger, S. Witte, Dielectric dispersion of ferroelectric ceramics and single crystals at microwave frequencies. *Ann. Phys.* **3**, 578–588 (1994).
10. A. S. Sidorkin, Translational vibrations of domain structure in ferroelectrics. *J. Appl. Phys.* **83**, 3762–3768 (1998).
11. J. de Los S. Guerra, J. A. Eiras, Mechanical and electrical driving field induced high-frequency dielectric anomalies in ferroelectric systems. *J. Phys. Condens. Matter* **19**, 386217 (2007).
12. V. Porokhonskyy, L. Jin, D. Damjanovic, Separation of piezoelectric grain resonance and domain wall dispersion in $Pb(Zr,Ti)O_3$ ceramics. *Appl. Phys. Lett.* **94**, 212906 (2009).
13. F. Kremer, A. Schonhals, W. Luck, *Broadband Dielectric Spectroscopy* (Springer, 2002).
14. S. Gevorgian, *Ferroelectrics in Microwave Devices, Circuits and Systems: Physics, Modeling, Fabrication and Measurements* (Springer, 2009).
15. G. Catalan, J. Seidel, R. Ramesh, J. F. Scott, Domain wall nanoelectronics. *Rev. Mod. Phys.* **84**, 119–156 (2012).
16. J. Seidel, L. W. Martin, Q. He, Q. Zhan, Y.-H. Chu, A. Rother, M. E. Hawkridge, P. Maksymovych, P. Yu, M. Gajek, N. Balke, S. V. Kalinin, S. Gemming, F. Wang, G. Catalan, J. F. Scott, N. A. Spaldin, J. Orenstein, R. Ramesh, Conduction at domain walls in oxide multiferroics. *Nat. Mater.* **8**, 229–234 (2009).
17. J. Guyonnet, I. Gaponenko, S. Gariglio, P. Paruch, Conduction at domain walls in insulating $Pb(Zr_{0.2}Ti_{0.8})O_3$ thin films. *Adv. Mater.* **23**, 5377–5382 (2011).
18. M. Schröder, A. Haußmann, A. Thiessen, E. Soergel, T. Woike, L. M. Eng, Conducting domain walls in lithium niobate single crystals. *Adv. Funct. Mater.* **22**, 3936–3944 (2012).
19. R. K. Vasudevan, W. Wu, J. R. Guest, A. P. Baddorf, A. N. Morozovska, E. A. Eliseev, N. Balke, V. Nagarajan, P. Maksymovych, S. V. Kalinin, Domain wall conduction and polarization-mediated transport in ferroelectrics. *Adv. Funct. Mater.* **23**, 2592–2616 (2013).
20. T. Sluka, A. K. Tagantsev, P. Bednyakov, N. Setter, Free-electron gas at charged domain walls in insulating $BaTiO_3$. *Nat. Commun.* **4**, 1808 (2013).
21. Y. S. Oh, X. Luo, F.-T. Huang, Y. Wang, S.-W. Cheong, Experimental demonstration of hybrid improper ferroelectricity and the presence of abundant charged walls in $(Ca,Sr)_3Ti_2O_7$ crystals. *Nat. Mater.* **14**, 407–413 (2015).
22. A. Crassous, T. Sluka, A. K. Tagantsev, N. Setter, Polarization charge as a reconfigurable quasi-dopant in ferroelectric thin films. *Nat. Nanotechnol.* **10**, 614–618 (2015).
23. M. Y. Gureev, A. K. Tagantsev, N. Setter, Head-to-head and tail-to-tail 180° domain walls in an isolated ferroelectric. *Phys. Rev. B* **83**, 184104 (2011).
24. E. A. Eliseev, A. N. Morozovska, G. S. Svechnikov, V. Gopalan, V. Ya. Shur, Static conductivity of charged domain walls in uniaxial ferroelectric semiconductors. *Phys. Rev. B* **83**, 235313 (2011).
25. E. A. Eliseev, A. N. Morozovska, Y. Gu, A. Y. Borisevich, L.-Q. Chen, V. Gopalan, S. V. Kalinin, Conductivity of twin-domain-wall/surface junctions in ferroelastics: Interplay of deformation potential, octahedral rotations, improper ferroelectricity, and flexoelectric coupling. *Phys. Rev. B* **86**, 085416 (2012).
26. Y. Du, X. L. Wang, D. P. Chen, S. X. Dou, Z. X. Cheng, M. Higgins, G. Wallace, J. Y. Wang, Domain wall conductivity in oxygen deficient multiferroic $YMnO_3$ single crystals. *Appl. Phys. Lett.* **99**, 252107 (2011).
27. Y. Du, X. Wang, D. Chen, Y. Yu, W. Hao, Z. Cheng, S. X. Dou, Manipulation of domain wall mobility by oxygen vacancy ordering in multiferroic $YMnO_3$. *Phys. Chem. Chem. Phys.* **15**, 20010–20015 (2013).
28. S. H. Skjærvø, E. T. Wefring, S. K. Nesdal, N. H. Gaukås, G. H. Olsen, J. Glaum, T. Tybell, S. M. Selbach, Interstitial oxygen as a source of *p*-type conductivity in hexagonal manganites. *Nat. Commun.* **7**, 13745 (2016).
29. J. Seidel, P. Maksymovych, Y. Batra, A. Katan, S.-Y. Yang, Q. He, A. P. Baddorf, S. V. Kalinin, C.-H. Yang, J.-C. Yang, Y.-H. Chu, E. K. H. Salje, H. Wormeester, M. Salmeron, R. Ramesh, Domain wall conductivity in La-doped $BiFeO_3$. *Phys. Rev. Lett.* **105**, 197603 (2010).
30. B. B. Van Aken, T. T. M. Palstra, A. Filippetti, N. A. Spaldin, The origin of ferroelectricity in magnetoelectric $YMnO_3$. *Nat. Mater.* **3**, 164–170 (2004).
31. T. Choi, Y. Horibe, H. T. Yi, Y. J. Choi, W. Wu, S.-W. Cheong, Insulating interlocked ferroelectric and structural antiphase domain walls in multiferroic $YMnO_3$. *Nat. Mater.* **9**, 253–258 (2010).
32. Y. Kumagai, N. A. Spaldin, Structural domain walls in polar hexagonal manganites. *Nat. Commun.* **4**, 1540 (2013).
33. G. V. Subba Rao, B. M. Wanklyn, C. N. R. Rao, Electrical transport in rare earth ortho-chromites, -manganites and -ferrites. *J. Phys. Chem. Solids* **32**, 345–358 (1971).
34. W. Wu, J. R. Guest, Y. Horibe, S. Park, T. Choi, S.-W. Cheong, M. Bode, Polarization-modulated rectification at ferroelectric surfaces. *Phys. Rev. Lett.* **104**, 217601 (2010).
35. K. Lai, W. Kundhikanjana, M. A. Kelly, Z.-X. Shen, Nanoscale microwave microscopy using shielded cantilever probes. *Appl. Nanosci.* **1**, 13–18 (2011).
36. K. Lai, W. Kundhikanjana, M. A. Kelly, Z.-X. Shen, Modeling and characterization of a cantilever-based near-field scanning microwave impedance microscope. *Rev. Sci. Instrum.* **79**, 063703 (2008).
37. Q. Zhang, G. Tan, L. Gu, Y. Yao, C. Jin, Y. Wang, X. Duan, R. Yu, Direct observation of multiferroic vortex domains in $YMnO_3$. *Sci. Rep.* **3**, 2741 (2013).
38. S. C. Chae, Y. Horibe, D. Y. Jeong, N. Lee, K. Iida, M. Tanimura, S.-W. Cheong, Evolution of the domain topology in a ferroelectric. *Phys. Rev. Lett.* **110**, 167601 (2013).
39. A. Tselev, P. Yu, Y. Cao, L. R. Dedon, L. W. Martin, S. V. Kalinin, P. Maksymovych, Microwave a.c. conductivity of domain walls in ferroelectric thin films. *Nat. Commun.* **7**, 11630 (2016).
40. E. Y. Ma, Y.-T. Cui, K. Ueda, S. Tang, K. Chen, N. Tamura, P. M. Wu, J. Fujioka, Y. Tokura, Z.-X. Shen, Mobile metallic domain walls in an all-in-all-out magnetic insulator. *Science* **350**, 538–541 (2015).
41. S.-Z. Lin, X. Wang, Y. Kamiya, G.-W. Chern, F. Fan, D. Fan, B. Casas, Y. Liu, V. Kiryukhin, W. H. Zurek, C. D. Batista, S.-W. Cheong, Topological defects as relics of emergent continuous symmetry and Higgs condensation of disorder in ferroelectrics. *Nat. Phys.* **10**, 970–977 (2014).
42. D. Meier, J. Seidel, A. Cano, K. Delaney, Y. Kumagai, M. Mostovoy, N. A. Spaldin, R. Ramesh, M. Fiebig, Anisotropic conductance at improper ferroelectric domain walls. *Nat. Mater.* **11**, 284–288 (2012).
43. W. Wu, Y. Horibe, N. Lee, S.-W. Cheong, J. R. Guest, Conduction of topologically protected charged ferroelectric domain walls. *Phys. Rev. Lett.* **108**, 077203 (2012).
44. S. Artyukhin, K. T. Delaney, N. A. Spaldin, M. Mostovoy, Landau theory of topological defects in multiferroic hexagonal manganites. *Nat. Mater.* **13**, 42–49 (2014).
45. K. Z. Rushchanskii, M. Ležaić, Ab initio phonon structure of *h*-$YMnO_3$ in low-symmetry ferroelectric phase. *Ferroelectrics* **426**, 90–96 (2012).
46. R. E. Peierls, The size of a dislocation. *Proc. Phys. Soc.* **52**, 34–43 (1940).
47. F. R. N. Nabarro, Dislocations in a simple cubic lattice. *Proc. Phys. Soc.* **59**, 256–272 (1947).
48. M. Methfessel, Elastic constants and phonon frequencies of Si calculated by a fast full-potential linear-muffin-tin-orbital method. *Phys. Rev. B* **38**, 1537–1540 (1988).
49. X.-B. Chen, N. T. M. Hien, K. Han, J.-Y. Nam, N. T. Huyen, S.-I. Shin, X. Wang, S. W. Cheong, D. Lee, T. W. Noh, N. H. Sung, B. K. Cho, I.-S. Yang, Study of spin-ordering and spin-reorientation transitions in hexagonal manganites through Raman spectroscopy. *Sci. Rep.* **5**, 13366 (2015).
50. F. Garcia-Sanchez, P. Borys, R. Soucaille, J.-P. Adam, R. L. Stamps, J.-V. Kim, Narrow magnonic waveguides based on domain walls. *Phys. Rev. Lett.* **114**, 247206 (2015).
51. S. Datta, *Surface Acoustic Wave Devices* (Prentice Hall, 1986).
52. M.-G. Han, Y. Zhu, L. Wu, T. Aoki, V. Volkov, X. Wang, S. C. Chae, Y. S. Oh, S.-W. Cheong, Ferroelectric switching dynamics of topological vortex domains in a hexagonal manganite. *Adv. Mater.* **25**, 2415–2421 (2013).
53. D. G. Tomuta, S. Ramakrishnan, G. J. Nieuwenhuys, J. A. Mydosh, The magnetic susceptibility, specific heat and dielectric constant of hexagonal $YMnO_3$, $LuMnO_3$ and $ScMnO_3$. *J. Phys. Condens. Matter* **13**, 4543 (2001).
54. A. K. Jonscher, Dielectric relaxation in solids. *J. Phys. D Appl. Phys.* **32**, R57–R70 (1999).
55. P. E. Blöchl, Projector augmented-wave method. *Phys. Rev. B* **50**, 17953–17979 (1994).
56. P. Giannozzi, S. Baroni, N. Bonini, M. Calandra, R. Car, C. Cavazzoni, D. Ceresoli, G. L. Chiarotti, M. Cococcioni, I. Dabo, A. Dal Corso, S. de Gironcoli, S. Fabris, G. Fratesi,

R. Gebauer, U. Gerstmann, C. Gougoussis, A. Kokalj, M. Lazzeri, L. Martin-Samos, N. Marzari, F. Mauri, R. Mazzarello, S. Paolini, A. Pasquarello, L. Paulatto, C. Sbraccia, S. Scandolo, G. Sclauzero, A. P. Seitsonen, A. Smogunov, P. Umari, R. M. Wentzcovitch, QUANTUM ESPRESSO: A modular and open-source software project for quantum simulations of materials. *J. Phys. Condens. Matter* **21**, 395502 (2009).

57. C. J. Fennie, K. M. Rabe, Ferroelectric transition in $YMnO_3$ from first principles. *Phys. Rev. B* **72**, 100103 (2005).

Acknowledgments: We thank W. Wu for helpful discussions. **Funding:** The SIM work was supported by the NSF Division of Materials Research (Award 1649490). The instrumentation was supported by the U.S. Army Research Laboratory and the U.S. Army Research Office under grant W911NF1410483. The work at Rutgers is funded by the Gordon and Betty Moore Foundation's Emergent Phenomena in Quantum Systems (EPiQS) Initiative through grant GBMF4413 to the Rutgers Center for Emergent Materials. **Author contributions:** S.-W.C. and K.L. conceived and designed the experiments. R.H. grew the materials. X.W., L.Z., and Y.R. constructed the electronics and performed the SIM experiment and numerical analysis. U.P. and S.A. performed the theoretical studies. X.W., S.A., and K.L. wrote the initial draft of the paper. All authors were involved in the discussion of results and edited the manuscript. **Competing interests:** The authors declare that they have no competing interests. **Data and materials availability:** All data needed to evaluate the conclusions in the paper are present in the paper and/or the Supplementary Materials. Additional data related to this paper may be requested from the authors.

Submitted 28 September 2016
Accepted 3 March 2017
Published 10 May 2017
10.1126/sciadv.1602371

Citation: X. Wu, U. Petralanda, L. Zheng, Y. Ren, R. Hu, S.-W. Cheong, S. Artyukhin, K. Lai, Low-energy structural dynamics of ferroelectric domain walls in hexagonal rare-earth manganites. *Sci. Adv.* **3**, e1602371 (2017).